JOURNAL OF BIOMEDICAL OPTICS 2(3), 251–261 (JULY 1997)

LIMITATIONS IN MEASUREMENT OF SUBSURFACE TEMPERATURES USING PULSED PHOTOTHERMAL RADIOMETRY

Ujwal S. Sathyam[†‡] and Scott A. Prahl[†*‡]

[†]Oregon Medical Laser Center, Portland, Oregon 97225; [‡]Oregon Graduate Institute, Portland, Oregon 97291; *Oregon Health Sciences University, Portland, Oregon 97201

(Paper JBO-094 received May 16, 1996; revised manuscript received Jan. 16, 1997; accepted for publication Apr. 4, 1997.)

ABSTRACT

A pulsed photothermal technique to calculate internal temperatures from noncontact surface temperature measurements is presented. The inversion process is based on approximating the integral equation describing the thermal interaction with a matrix equation. The matrix equation is then solved using singular-value decomposition. The method was evaluated using computer simulations and experiments with tissue phantoms and skin. The algorithm predicted internal temperatures within 10% for homogeneous samples down to a depth of about 500 μm. It did not predict internal temperatures accurately for inhomogeneous samples, but yielded fairly accurate estimates of the depths of subsurface absorbers and conserved energy. The uncertainty in the calculated depth of the absorber increased with depth. Currently this technique can probe depths to 500 μm. © *1997 Society of Photo-Optical Instrumentation Engineers.* [S1083-3668(97)00103-2]

Keywords absorbing, scattering, temperature, buried, depth, infrared, black body radiation, layer, inverse.

1 INTRODUCTION

The success of many types of phototherapy depends on the distribution of light and subsequent heating within the tissue. Numerous models have been developed to predict the behavior of light in turbid media such as tissue. These usually assume the sample has uniform optical properties to make analytic solutions tractable. Also, often *a priori* knowledge of the optical properties of the tissue is required before the models can be used.

Real biological samples are heterogeneous structures, and many times one has no *a priori* knowledge of their optical properties. Skin is a layered structure: a thin stratum corneum resting on the epidermis that in turn sits on the dermis. Blood vessels, hair follicles, and melanin granules are distributed throughout these layers. Knowledge of the light distribution in the skin can be useful to many applications in dermatology, such as treatment of port wine stains and psoriasis, monitoring changes in thickness and concentration of topically applied medicines, and studying photoprotective mechanisms of the skin.

This paper describes a technique for extracting the initial internal temperature profile from the surface temperature following irradiation by a laser pulse (Figure 1). The technique is based on pulsed photothermal radiometry (PPTR) in which an optical pulse is used to induce a temperature perturbation within the sample. The transient thermal emission from the surface is monitored with an infrared detector. The surface temperature as a function of time is then used to calculate the internal temperature distribution as a function of depth immediately after the laser pulse. Such inverse problems in heat transfer are generally ill posed and require numerical methods to arrive at a solution.[1] The inversion algorithm presented here uses singular-value decomposition to solve a least-squares problem.

An important advantage of PPTR over other methods is that the measurement is made without touching the sample. For example, simply resting a probe on the surface of the skin for several seconds will change the hydration characteristics of the stratum corneum.[2] Slightly heavier contact will change the blood flow to the area under the probe, and is readily seen as blanching of the skin.

PPTR has been used extensively with nonbiological materials such as rubber and plastics to measure their thermal properties.[3–5] The technique has been used on biological samples and tissue phantoms to determine absorption and scattering coefficients.[6–9] PPTR of laminated materials and skin has been investigated to obtain information about the subsurface structure and thermophysical properties of the material.[10–12] Long et al. studied the delayed thermal waves arising from bruised skin *in vivo* using a simple two-layer absorption model.[13] The depth of

Address all correspondence to Scott A. Prahl, Oregon Medical Laser Center, 9205 SW Barnes Road, Portland, OR 97225. Tel: (503) 291-2109; Fax: (503) 291-2422; E-mail: prahl@ee.ogi.edu Current affiliation of Ujwal Sathyam: Lawrence Livermore Laboratories.

1083-3668/97/$10.00 © 1997 SPIE

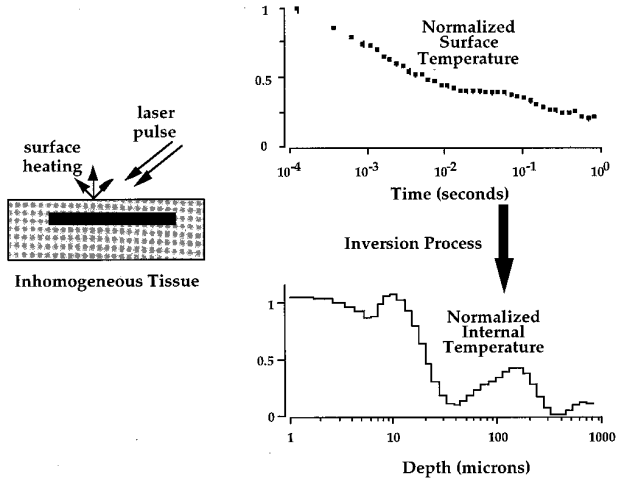

Fig. 1 The PPTR problem: A laser pulse thermally excites a semi-infinite material. The surface temperature is measured using an infrared detector. The goal is to convert surface temperatures as a function of time to initial temperatures as a function of depth immediately after the laser pulse.

the absorbing layer was calculated from the time of the maximum surface temperature. This work was recently extended to a two-layer scattering and absorbing model that more accurately simulated skin.[14] These studies all require relatively simple geometries and rigorous analytical treatment of the light transport in the sample. Furthermore, some *a priori* knowledge of the number of layers or their depths is needed.

Milner et al. and Jacques et al. approached the inverse problem by identifying the surface temperature as a convolution integral of a Green's function with the unknown internal temperature distribution.[15–17] The integral was then solved using a combination of iterative and least-squares algorithms. This technique was used to image port wine stains and to determine the thermal diffusivity of biomaterials. An important advantage is that no *a priori* knowledge about the sample is necessary.

We consider the problem of a turbid medium, either homogeneous or made of multiple absorbing and scattering layers. An inversion algorithm is used to convert the surface temperature as a function of time $T(0,t)$ to the internal temperature distribution $T(z,0)$ immediately after the laser pulse. The depths of buried absorbing layers are then correlated with peaks in the calculated internal temperature. The algorithm uses a matrix formulation to solve the heat transfer problem directly. The effect of infrared absorption from points within the sample is also incorporated into the analysis. The technique is fast and uses standard matrix manipulations. In a recent report, Milner et al. considered the same problem and used numerical methods to solve the inverse heat transfer problem.[18] We use a slightly different numerical inversion technique to solve the matrix equation.

The algorithm is tested with data from known thermal distributions, both simulated and measurements from controlled gel phantoms. Finally it is tested on human skin *in vivo*, including both healthy skin and that with port wine stains. The limitations of this technique are that absorption profiles can only be made to a depth of 500 μm before the signal decays too much. Fortunately, most interesting structures in the skin are found between 0 and 600 μm from the surface.[19] The uncertainty in the location of the internal temperature layers increases with the depth of the layer.

2 THEORY

The goal is to convert the surface temperature $T(0,t)$ as a function of time to an initial temperature distribution $T(z,0)$ as a function of depth without *a priori* knowledge of the location or strength of the absorbers (Figure 1). The sample is assumed to be semi-infinite and to have uniform thermal properties. The thermal boundary condition at the surface is assumed to be adiabatic and the problem is constrained to be one dimensional. Practically, this requires a relatively large laser spot so that radial heat diffusion can be ignored. Also, the pulse duration should be short enough to ignore heat losses at the surface.

The algorithm is based on solving a purely inverse heat transfer problem. The surface radiometric signal $S(t)$ at any time t is the sum of the contributions from all depths in the tissue at time t. However, the radiation from deeper depths is attenuated by the infrared absorption of the sample before reaching the detector. This is stated mathematically by Eq. (1).

$$S(t)=\epsilon\eta a_D\sigma\int_0^\infty [T(z,t)^4-T_0^4]\exp(-\mu_{\mathrm{IR}}z)\mu_{\mathrm{IR}}dz. \tag{1}$$

$T(z,t)-T_0$ is the rise in temperature at depth z and time t. η is the detector efficiency (incorporating both the sensitivity and collection efficiencies), a_D is the detector area, and σ is the Stefan–Boltzmann constant. The exponential factor accounts for the attenuation of the radiations from deeper depths. Average values for η, ϵ, and μ_{IR} over the range of detection are used.

Equation (1) assumes that the infrared detection system is collecting radiation and is responsive over an infinite bandwidth. Most physical thermal detection systems operate in either the 3 to 5 μm or in the 8 to 12 μm waveband. This study has utilized an HgCdTe detector operating in the 8 to 12 μm region. Therefore in principle, the effect of a band-limited detection should be incorporated into the theory. However, the radiated emissive power in the 8 to 12 μm waveband has a distribution similar to that of the wide-band emissive power for a temperature range of 0 to 100 °C with a scaling factor of

about 0.26.[20] This factor of 0.26 is easily incorporated mathematically into the detector efficiency η. Another point to be noted is that the surface emissivity is not explicitly present in Eq. (1) since the irradiated material is not in radiative thermal equilibrium. Rather, its effect is accounted for by the depth integral of the exponent and the infrared absorption.

The problem now is to extract $\Delta T(z,t)=T(z,t)-T_0$ from $S(t)$. One approach is to assume that the initial signal immediately after the laser pulse is influenced only by the initial temperature at the surface, with no contributions from deeper depths. This assumption is valid if the infrared absorption of the tissue is very high so that radiation from deeper depths can be ignored. After a short time (say 5 ms), heat can diffuse only a short distance ($\approx 5\ \mu$m), contributing to the signal at 5 ms after the laser pulse. Since the initial surface temperature is known, the initial temperature of a thin layer just below the surface can be determined. Jacques et al. developed an iterative algorithm based on the above principle and applied it to port wine stain lesions of human skin.[16] This method, however, overestimates the temperatures at the depths near the surface when the infrared absorption is not very high.

2.1 FORMULATION

We formulate the heat transfer problem as a first-order Fredholm integral equation. The kernel of the equation is determined by the Green's function for a layer source of heat located at various depths in the tissue. The effect of a finite infrared absorption ($\sim 1200\ \mathrm{cm}^{-1}$) is also incorporated into the kernel. We then make a matrix approximation and convert the integral equation to a least-squares problem that is solved using singular-value decomposition. The algorithm does not use an iterative process. Once the singular-value decomposition of the kernel has been accomplished, the initial temperature distribution is generated by a single matrix multiplication.

If the temperature rise $[T(z,t)-T_0]$ is small, the bracketed quantity in (1) can be expanded using the binomial theorem. Neglecting terms of $O([T(z,t)-T_0]^2)$ and higher yields

$$S(t)=4\eta a_D \epsilon \sigma T_0^3 \int_0^\infty [T(z,t)-T_0]\exp(-\mu_{\mathrm{IR}} z)\mu_{\mathrm{IR}} dz. \tag{2}$$

The temperature rise $\Delta T(z,t)=T(z,t)-T_0$ at any time following the laser pulse is a convolution of the appropriate Green's function with the temperature rise $\Delta T(z,0)=T(z,0)-T_0$ immediately after the laser pulse,[21]

$$\Delta T(z,t)=\int_0^\infty \Delta T(z',0)G(z',t'=0;z,t)dz'. \tag{3}$$

$G(z',t'=0;z,t)$ is the Green's function for an instantaneous planar source of heat located at a depth z' and released at time t' with an adiabatic boundary condition. Practically, an instantaneous source of heat requires a laser pulse duration much smaller than the thermal relaxation time of the sample.

Substituting Eq. (3) into Eq. (2) and after appropriate nondimensionalizing and normalization, an inhomogeneous Fredholm integral equation of the first kind can be written[22]:

$$s(\tau)=\int_0^\infty f(\zeta)K(\zeta,\tau)d\zeta$$

$$\zeta \equiv \mu_{\mathrm{IR}} z \quad \text{and} \quad \tau \equiv \mu_{\mathrm{IR}}{}^2 \kappa t, \tag{4}$$

where κ is the thermal diffusivity. The initial temperature distribution is redefined as

$$f(\zeta)\equiv \Delta T(\zeta,0). \tag{5}$$

The kernel $K(\zeta,\tau)$ in Eq. (4) is

$$K(\zeta',\tau)=\int_0^\infty G(\zeta',0;\zeta,\tau)\exp(-\zeta)d\zeta, \tag{6}$$

where $G(\zeta',0;\zeta,\tau)$ is the adiabatic Green's function for a planar source at depth ζ'.

$$G(\zeta',\tau'=0;\zeta,\tau)=\frac{1}{2\sqrt{\pi\tau}}\left\{\exp\left[-\frac{(\zeta-\zeta')^2}{4\tau}\right]+\exp\left[-\frac{(\zeta+\zeta')^2}{4\tau}\right]\right\}. \tag{7}$$

All the physics of the process is contained in the kernel; $s(\tau)$ is the measured surface signal and $f(\zeta)$ is the unknown internal temperature distribution.

2.2 SOLUTION

The Fredholm integral equation (4) is solved by approximating the integral as a sum. This involves discretization of both depth (N depths) and time (M times). The integral for the surface temperature may be approximated by matrix equation:

$$s(\tau_j)\approx \sum_{i=1}^{N} K(\zeta_i,\tau_j)f(\zeta_i)\Delta\zeta_i. \tag{8}$$

The above equation is solved by singular-value decomposition of the kernel **K** and approximation of **K** using a Levenberg–Marquardt method.[22] The entire description of the numerical inversion is too complex to be described in this paper. The interested reader is referred to excellent treatments in Press et al.[23] and Lawson and Hanson.[24] However, the salient features of the numerical inversion are presented here. Typically, the number of radiometric measurements M greatly exceeds the number of

internal temperatures N that will be found. Equation (8) can therefore be solved using least-squares techniques. The formal solution can be written as

$$\mathbf{f}=\mathbf{K}^{-1}\ \mathrm{s}, \tag{9}$$

where the pseudoinverse $\mathbf{K}^{-1}$ is based on singular-value decomposition of $\mathbf{K}$

$$\mathbf{K}=\mathbf{u}^{T}\mathbf{m}\mathbf{v}. \tag{10}$$

Here $\mathbf{u}$ and $\mathbf{v}$ are two row orthonormal matrices, and $\mathbf{m}$ is a diagonal matrix. The pseudoinverse is defined as

$$\mathbf{K}^{-1}=\mathbf{v}^{T}\mathbf{m}^{-1}\mathbf{u}. \tag{11}$$

The initial temperature distribution $\mathbf{f}$ is then

$$\mathbf{f}=\mathbf{v}^{T}\mathbf{m}^{-1}\mathbf{u}\mathbf{s}. \tag{12}$$

The entries in the matrix $\mathbf{m}$ are the singular values of the matrix $\mathbf{K}$. The complete set of singular values m_i is required to satisfy the equality in Eq. (10). Since small singular values are associated with large $1/m_i$ entries in the inverse matrix $\mathbf{m}^{-1}$, they can cause huge oscillations and instabilities in the calculated solution vector. Particularly, any noise in the collected data will tend to get amplified. It is therefore necessary to mitigate the effects of these small singular values using some type of regularization technique.

The goal is to approximate the kernel matrix $\mathbf{K}$ sufficiently well that all the relevant physics is retained, and yet find an approximation that prevents the small singular values from amplifying the noise in the surface measurements. We employed the popular Levenberg–Marquardt method that smoothly attenuates effects of small singular values by introducing a parameter λ. The singular values are replaced by terms with the form $(m_i^2+\lambda^2)^{1/2}$. The regularization factor λ' in our algorithm varied between 0.005 and 0.02. This creates new matrices and vectors that satisfy

$$\mathbf{f}_{\lambda}=\mathbf{K}_{\lambda}^{-1}s_{\lambda} \tag{13}$$

and approximates the originals with increasing fidelity as $\lambda\rightarrow 0$. The optimum value of λ is determined by an L-curve analysis that computes the smallest λ that minimizes the Euclidean norm $\|\mathbf{s}-\mathbf{s}_{\lambda}\|$.[24] There are other regularization techniques available in the literature that can be also be employed. Milner et al. used the techniques of (1) truncating small singular values and (2) conjugate gradients.[18] All three regularization techniques seem to be fairly efficient at mitigating the effects of small singular values. However, one side effect of this smoothing process is that it also tends to smoothen any sharp transients in the unknown solution vector, as will be seen further in this paper. This effect was also observed by Milner et al.[18]

The first step involved in converting the integral equation (4) into the matrix equation (8) is the discretization of time and depth. To understand how quickly the surface temperature should be sampled, consider a plane source located at depth ζ. If both adiabatic boundary conditions and infrared penetration are ignored for simplicity, the change in temperature due to an instantaneous planar source released at time $\tau=0$ and depth ζ is

$$\Delta T(\tau)=\frac{Q}{2\sqrt{\pi\tau}}\exp\left[-\frac{\zeta^2}{4\tau}\right]. \tag{14}$$

The characteristic time at which the maximum occurs is

$$\tau_c=\frac{\zeta^2}{2}. \tag{15}$$

If there are two plane sources at ζ and $\zeta+\Delta\zeta$, the time interval between the two thermal maxima will be

$$\Delta\tau_c=\zeta\Delta\zeta+\frac{(\Delta\zeta)^2}{2}. \tag{16}$$

For a fixed separation $\Delta\zeta$, the time interval will be smallest when the two sources are close to the surface. The sampling theorem dictates that the sampling rate must be at least twice this fast to resolve individual sources. The theoretical resolution in depth based on a sampling interval of τ_{samp} is therefore

$$\Delta\zeta_{\min}\approx\sqrt{4\Delta\tau_{\mathrm{samp}}}. \tag{17}$$

The above relation is primarily useful in determining the location of the first depth $\zeta_1=\Delta\zeta_{\min}$. The maximum signal reaching the surface from a buried source decreases with increasing depth of the source.

$$\Delta T_{\max}\propto\zeta^{-1}. \tag{18}$$

Therefore, to detect a signal from a depth ζ as well as one from near the surface, samples must be averaged, and the number of averaged points must increase proportional to ζ. This means that the spacing of internal depths should not be uniform: the spacing should be smaller close to the surface. This may be achieved by letting the spacing increase geometrically

$$\zeta_{i+1}=(1+\alpha)^{i}\zeta_1, \tag{19}$$

where α is a positive constant that will depend on the number of internal temperatures to be calculated, the depth of the shallowest point, and the depth of the deepest point. The final depth may be determined according to the last sampling time [Eq. (15)]. Note that the ζ_is will be distributed uniformly when plotted on a logarithmic scale. The factor α is then determined as

$$\alpha=\left[\frac{\zeta_N}{\zeta_1}\right]^{1/N-1}-1 \tag{20}$$

once the number of internal temperature points N to be calculated has been chosen.

3 MATERIALS AND METHODS

The inversion algorithm was tested was evaluated using data from computer simulations and experiments with tissue phantoms and human skin. Initially, homogeneous samples of known optical properties were used so that analytic solutions for the internal temperature distribution could be used for evaluating the algorithm. Next, computer-generated and experimental data from layered inhomogeneous samples were used. Finally, the technique was applied to human skin, both healthy and with port wine stains. All the calculations in this paper assumed that the diffusivity κ of the irradiated material was equal to that of water ($0.0014\ \mathrm{cm^2/s}$). Since the infrared detector used in this study had a range of 8 to 12 μm, we used a weighted infrared absorption coefficient μ_{IR} for water ($1200\ \mathrm{cm^{-1}}$) over the detection range.

Four hundred surface temperature points were generated for each computer simulation; 10,000 points were collected with each experiment. These were all averaged to about 40 points uniformly spaced logarithmically in time between 1 μs and 1 s. The number of internal temperature points calculated was either 20 or 40, but never more than the number of averaged surface temperature points (this was to maintain $M>N$ in the matrix formulation). The depths were chosen so that they were uniformly distributed on a log scale between 1 and 1000 microns.

3.1 COMPUTER SIMULATIONS

The first computer simulations assumed homogeneous samples: absorbing-only and turbid. The initial internal temperature distribution for an absorbing-only sample is given by Beer's law:

$$f(\zeta)=T(\zeta,0)=\frac{E_0\mu_a}{\rho c}\exp(-\gamma\zeta), \tag{21}$$

where $\gamma=\mu_a/\mu_{\mathrm{IR}}$, μ_a is the absorption coefficient, E_0 is the radiant exposure reduced by any losses due to specular reflection from the surface, and ρc is the volumetric specific heat of the sample. The internal temperature distribution for a turbid sample with absorption μ_a and isotropic scattering μ_s is given by diffusion theory[24,28]

$$f(\zeta)=T(\zeta,0)=\frac{E_0\mu_a}{\rho c}\left[A\ \exp(-\gamma_{\mathrm{eff}}\zeta)+B\ \exp(-\gamma_{tr}\zeta)\right], \tag{22}$$

where $(\gamma_{\mathrm{eff}}=\mu_{\mathrm{eff}}/\mu_{\mathrm{IR}})$; $(\gamma_{tr}=\mu_{tr}/\mu_{\mathrm{IR}})$; $(\mu_{tr}=\mu_a+\mu_s)$; $(\mu_{\mathrm{eff}}=\sqrt{3\mu_{tr}\mu_a})$; and coefficients A and B are determined by diffusion theory.

The surface temperatures for absorbing-only and turbid samples are obtained by substituting Eqs. (21) and (22) into Eq. (4), and using the Green's function for a planar adiabatic source. After suitable normalization to incident radiant exposure and initial temperature, this yields:

$$s(\tau)=\frac{\gamma}{1-\gamma^2}\left[\exp(\gamma^2\tau)\mathrm{erfc}(\gamma\sqrt{\tau})-\gamma\exp(\tau)\mathrm{erfc}(\sqrt{\tau})\right] \tag{23}$$

for an absorbing-only sample and

$$s(\tau)=\gamma\left(\frac{A}{1-\gamma_{\mathrm{eff}}^2}\left[\exp(\gamma_{\mathrm{eff}}^2\tau)\mathrm{erfc}(\gamma_{\mathrm{eff}}\sqrt{\tau})-\gamma_{\mathrm{eff}}\exp(\tau)\mathrm{erfc}(\sqrt{\tau})\right]+\frac{B}{1-\gamma_{tr}^2}\left[\exp(\gamma_{tr}^2\tau)\mathrm{erfc}(\gamma_{tr}\sqrt{\tau})-\gamma_{tr}\exp(\tau)\mathrm{erfc}(\sqrt{\tau})\right]\right) \tag{24}$$

for a turbid sample; $\mathrm{erfc}(x)$ is the complementary error function. Surface temperature values were generated using Eqs. (23) and (24) and fed into the inversion algorithm. The internal temperature values generated were compared with theory given by Eqs. (21) and (22). The values for μ_a and μ_s used in the simulation were $\mu_a=10\ \mathrm{cm^{-1}}$ for absorbing-only samples and $\mu_a=20\ \mathrm{cm^{-1}}$, $\mu_s=50\ \mathrm{cm^{-1}}$ for turbid samples.

Next, the algorithm was tested on simulated radiometric signals from an inhomogeneous material. Surface temperature data for an instantaneously heated unit planar impulse buried at depths of 10, 50, 100, and 500 μm were generated. A planar source buried at depth ζ_0 was represented by a delta function $f(\zeta)=\delta(\zeta-\zeta_0)$. Substituting this delta function into Eq. (4) and using (6) and (7), we get:

$$s(\tau)=K_{\mathrm{plane}}(\zeta_0,\tau)=\frac{1}{2}\exp(\tau-\zeta_0)\mathrm{erfc}\left(\sqrt{\tau}-\frac{\zeta_0}{2\sqrt{\tau}}\right)+\frac{1}{2}\exp(\tau+\zeta_0)\mathrm{erfc}\left(\sqrt{\tau}+\frac{\zeta_0}{2\sqrt{\tau}}\right), \tag{25}$$

where ζ_0 is the depth of the planar impulse. The next set of simulations was done with two plane

sources at depths ζ_1 and ζ_2. The radiometric signal was calculated using the principle of superposition.

$$s(\tau) = K_{\text{plane}}(\zeta_1, \tau) + K_{\text{plane}}(\zeta_2, \tau). \quad (26)$$

The depths of the impulses varied between 10 and 500 μm.

3.2 TISSUE PHANTOMS

The homogeneous phantoms were gelatin (Sigma Chemicals) with black India ink (Faber-Castell, No. 4415) as the absorber and Intralipid-20% (Clinton Nutrition Co., Deerfield, Illinois) as the scatterer. Homogeneous samples were prepared by heating a 5% weight by volume solution of gel and adding India ink and Intralipid in appropriate amounts to achieve the desired absorption and scattering coefficients, and then allowing the mixture to solidify in rectangular plastic molds ($30\times75\times5$ mm). The absorption coefficient was measured on a spectrophotometer (8452A, Hewlett Packard) before addition of Intralipid and gelling. Since Intralipid is not an isotropic scatterer (anisotropy $g\sim0.8$), the reduced scattering coefficient $\mu_s' = \mu_s(1-g)$ was used. The reduced scattering coefficient (μ_s') of the gel was calculated using the relations given by van Staveren et al.[25] The absorption and reduced scattering coefficients were also independently verified using the PPTR method described by Prahl et al.[9] The values obtained by these methods were in good agreement within 5%. The absorption varied between 5 and 100 cm^{-1}, and reduced scattering varied between 0 and 100 cm^{-1}.

Inhomogeneous tissue phantoms were made by stacking thin gel layers with different absorption and scattering coefficients on a clear gel substrate. The thickness of each gel layer was 170 μm in initial experiments and then reduced to 70 μm in subsequent experiments. Polyacrylamide was used as the gel instead of gelatin since it proved to be difficult to make thin gelatin layers. A 20% polyacrylamide gel was prepared by mixing 9.735 g acrylamide and 0.265 g bis-acrylamide (Sigma Chemicals) in 50 ml water. Polymerization was initiated by 0.01 g ammonium persulfate in 0.5 ml water and 0.1 ml tetramethylethylenediamine (TEMED) (Sigma Chemicals). India ink and Intralipid were added in appropriate amounts before polymerization to achieve the desired absorption and reduced scattering coefficients.

Thin gel layers were obtained by quickly injecting the gel solution (after adding the initiators) between microscope slides separated by 70 or 170-μm spacers. After polymerization, the microscope slides were removed under water. The resulting gel layers were homogeneous and had a uniform thickness of 70 or 170 μm. The final layered sample was obtained by stacking the gel layers onto a previously prepared and polymerized clear gel substrate. Typically a finished phantom consisted of 1 to 8 gel layers on a ~3 mm clear gel substrate.

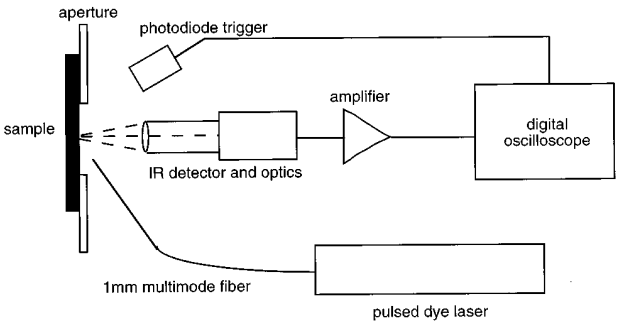

Fig. 2 Schematic diagram of experiment: The excitation source is a 1 μs pulsed dye laser at 506 nm for the tissue phantoms and 577 nm for skin. The surface emission is monitored by an infrared detector and the data are collected by a digital oscilloscope. The trigger source for the experiment is provided by a photodiode detecting the laser pulse.

Initial experiments with the inhomogeneous tissue phantom used only one absorbing layer ($\mu_a = 400$ cm^{-1}) of 170 μm thickness. The other layers were clear and no scattering was introduced. The absorbing layer was buried at various depths between 0 and 500 μm. An absorption of 400 cm^{-1} was chosen to approximate blood absorption at 577 nm, the chosen wavelength for treatment of port wine stains.

The next set of experiments used thinner layers (70 μm), and scattering and absorption were introduced into the layers above the ''blood model'' to more closely model skin. A typical epidermis model had an absorption of $\mu_a = 30$ cm^{-1} and a scattering of $\mu_s' = 30$ cm^{-1}. A typical dermis model had $\mu_a = 10$ cm^{-1} and $\mu_s' = 60$ cm^{-1}. Finally a port wine stain was modeled with $\mu_a = 300$ cm^{-1} and $\mu_s = 10$ cm^{-1}. These values were chosen based on various studies on the optical properties of human skin.[19,26,27,29] All scattering coefficients reported here are reduced scattering coefficients.

3.3 PULSED PHOTOTHERMAL RADIOMETRY

Figure 2 shows a schematic diagram of the experimental apparatus. The sample was covered by a plastic plate with a 15×20 mm aperture. The source of the optical pulse was a flashlamp-pumped tunable dye laser (Palomar Medical 3010), emitting 1-μs pulses at 506 nm. The light was coupled into a 1-mm diameter quartz multimode fiber, the output end of which was maintained about 15 mm from the sample surface at an angle of about 45°. This resulted in a uniform spot of about 20 mm^2 on the sample. The incident radiant exposure ranged from 5 to 10 mJ/mm^2. The energy output of the laser was measured with an energy meter (Molectron) and found to be stable within 5%.

The infrared thermal signal from the irradiated sample was monitored using a 1-mm^2 HgCdTe photoconductive detector (EG&G Judson) with a wavelength detection range of 8 to 12 μm. The

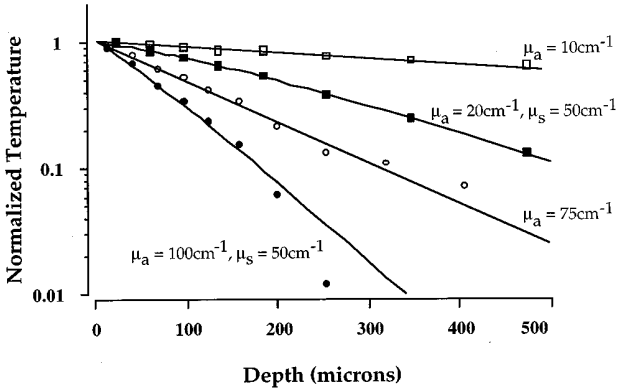

Fig. 3 The calculated internal temperature distribution for absorbing-only and turbid media. The solid curves represent analytical solutions for the internal temperature given by Beer's law for an absorbing-only and by diffusion theory for a turbid sample. The correspondence begins to fail when the predicted temperature is less than one-tenth of the maximum temperature. The temperatures are normalized to the maximum internal temperature.

1-mm^2 detector was placed at the focal plane of a germanium lens system with a conjugate ratio of 1:1. The detector signal was conditioned using a dc to 1.5-MHz amplifier impedance matched to the detector. The signal was then recorded on a digital oscilloscope. Typically the sampling rate was 10 to 50 μs/point and 10,000 data points were collected after the laser pulse. The trigger for the oscilloscope was provided by a photodiode detecting the laser pulse. The detector response was about 50 mV per degree Celsius rise in temperature. Ten pulses were averaged to reduce the noise.

3.4 SKIN EXPERIMENTS

Radiometric signals were collected from visibly healthy areas of the wrist and also from a port wine stain on the wrist of a Caucasian volunteer. The excitation source used in this case was a 577-nm, 1-μs pulsed dye laser. The laser energy was maintained at 100 mJ over an area of about 20 mm^2. Twenty pulses were averaged to reduce the noise.

4 RESULTS

4.1 COMPUTER SIMULATION

The results for a homogeneous sample are shown in Figure 3. The internal temperatures presented are normalized to the maximum signal at the surface. The data show excellent agreement between calculated symbols and expected curves. The expected curves are determined by Eq. (21) for a homogeneous absorbing sample and by Eq. (22) for a homogeneous turbid sample.

The next set of results for the computer-generated data is shown in Figure 4. Each histogram bar corresponds to one layer. The algorithm does a good job at roughly localizing the impulse, but the resolution is only 2 to 4 layers. Also, the height of the

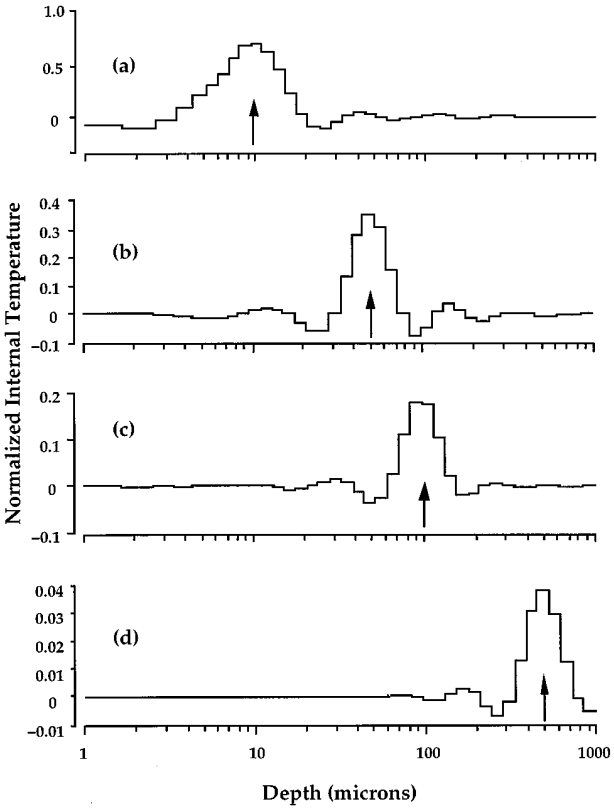

Fig. 4 The calculated internal temperature distribution for an impulse located at various depths as indicated by the arrows. The algorithm works well for identifying the depth of the impulse. The predicted width of the impulse increases with the depth. The height of the impulse decreases with increasing depth. The temperatures are normalized to the unit impulse used to generate the surface temperatures.

calculated impulse is less than the actual value at deeper depths. This implies that the prediction of real temperatures deteriorates with increasing depths.

The two-impulse results are shown in Figure 5. Again the location of the impulses is quite good. However, two impulses located close to each other (10 and 20 μm) could not be resolved. Impulses at 10 and 50 μm could be resolved. However, a similar source separation of 50 μm could not be resolved at deeper depths, as seen in Figure 5(c). This indicates that resolution deteriorates with increasing depth. Also, the height of the second impulse is less than that of the first, though impulses of equal amplitude were used to generate the surface temperatures. However, a comparison between Figures 4 and 5 shows that both impulses retain their amplitudes at the same depths; i.e., the second impulse at 50 μm in Figure 5(b) has the same height as the first impulse at 50 μm in Figure 5(c).

4.2 TISSUE PHANTOMS

Figure 6 shows the predicted internal temperature for homogeneous absorbing-only and turbid gel

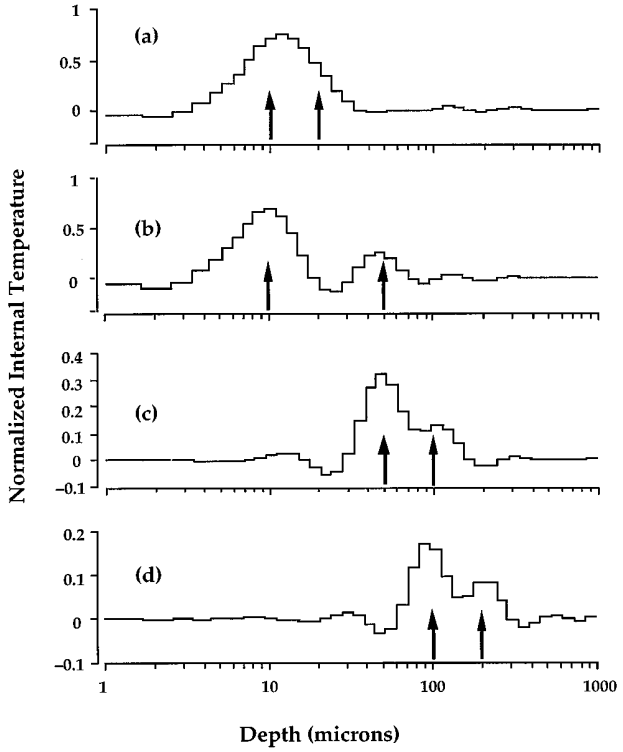

Fig. 5 The calculated internal temperature distribution for two impulses located at various depths as indicated by the arrows. The algorithm works well for identifying the depth of the impulses. The resolution between impulses improves with increasing spacing between the impulses. The magnitude of the second calculated impulse is less than that of the first. The temperatures are normalized to the unit impulse used to generate the surface temperatures.

samples. The data are shown normalized to the maximum temperature. Again there is excellent agreement between the calculated temperatures and theory. The correspondence begins to fail when

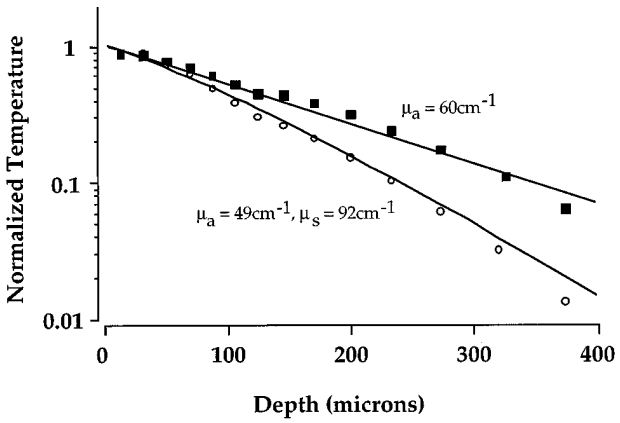

Fig. 6 The calculated internal temperature distribution for absorbing-only and turbid samples. The solid curves represent analytical solutions for the internal temperature given by Beer's law for an absorbing-only and by diffusion theory for a turbid sample. The predicted temperatures are accurate up to one-tenth of the maximum temperature. The temperatures are normalized to the maximum surface temperature detected.

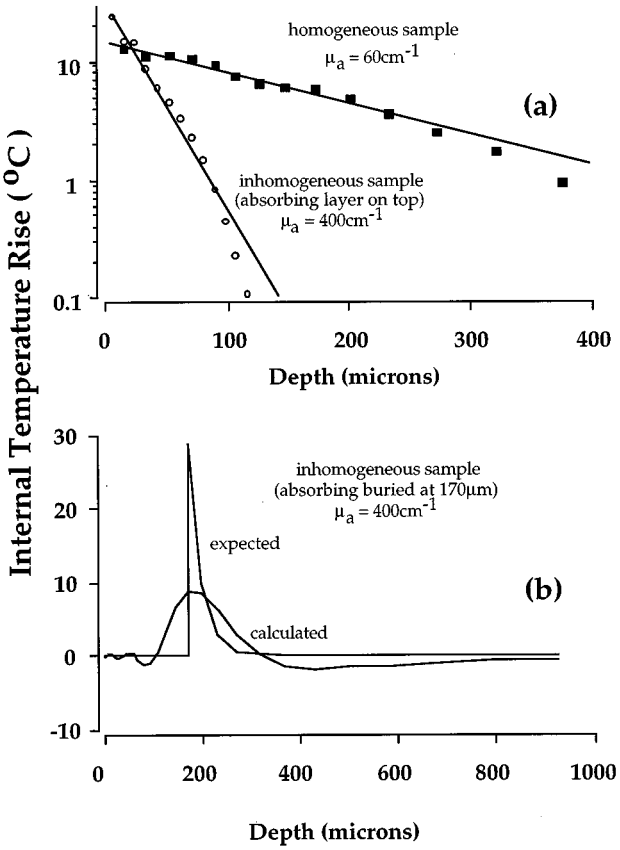

Fig. 7 Actual temperatures predicted by the algorithm. There is excellent agreement with theory for samples absorbing primarily at the surface, but the algorithm fails to predict actual temperatures when the principal absorber is buried. However, it is quite good at localizing the absorber.

the predicted temperature is less than one-tenth of the maximum temperature.

Real temperatures were calculated by dividing the predicted internal temperatures by the detector response. Figure 7 shows how well the algorithm does at predicting real temperatures for both homogeneous and layered samples. The predicted temperature profile for a buried layer is drastically attenuated and broadened. This is also evident in the buried impulse response shown in Figure 4. However, the algorithm does a reasonable job at locating the layer.

A change in surface signal could be detected for a maximum depth of 700 μm when there were no other absorbers on top of the layer. The predicted width of the layer increased with the depth of the layer. Figure 8 shows the calculated internal temperature profile for a gel layer buried at 170 and 510 μm under clear gel layers. The ability of the algorithm to predict real temperatures deteriorates with increasing depth of the absorbing layer. Also, more noise is introduced in the calculated temperature profile as the surface signal becomes weaker.

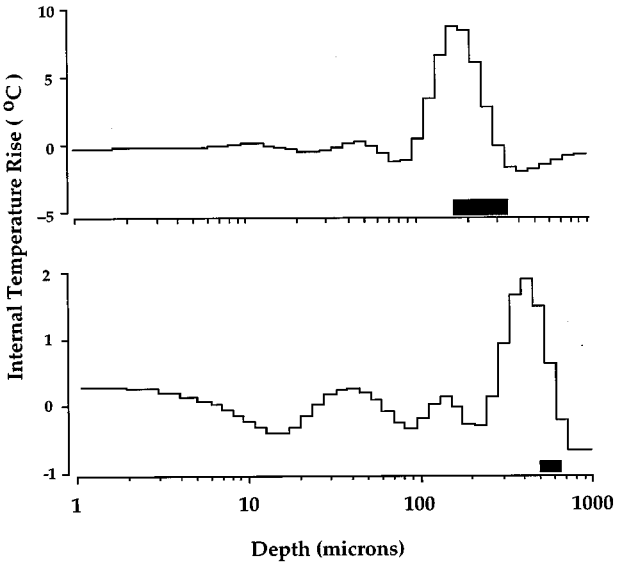

Fig. 8 The calculated internal temperature distribution for a 170 μm gel layer buried at 170 μm and 510 μm under clear gel layers. The layer is represented by the black bar below the temperature profiles. The absorption of the layer is 400 cm^{-1}. The algorithm works well for identifying the depth of the impulses, but does not do very well at predicting the magnitude of the temperature.

Figure 9 shows the results when scattering and absorption were introduced into the skin model. In Figure 9(a) a dip in the temperature profile is evident at around 70 μm, where the absorption profile changes from higher absorption ($\mu_a = 30\ cm^{-1}$) to lower absorption ($\mu_a = 10\ cm^{-1}$). The blood layer can be detected as a prominent peak at around 200 μm.

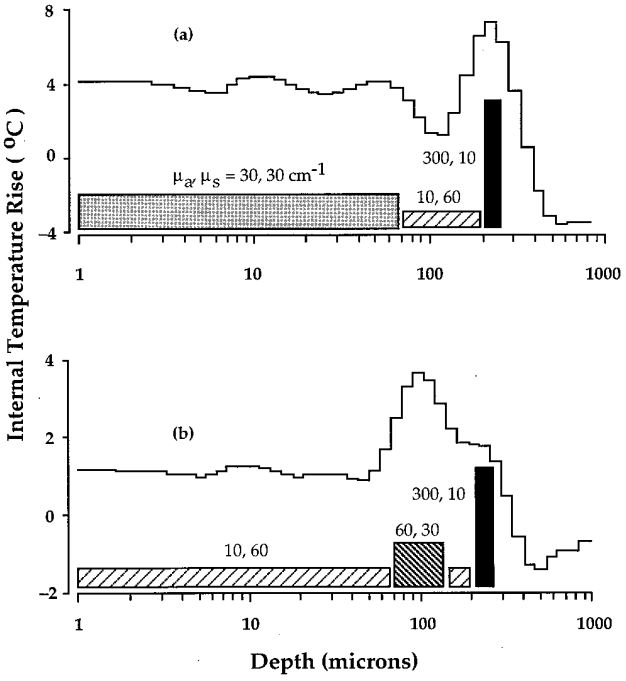

Fig. 9 Depth profiling for a gel-based skin model. The position and width of the layers are indicated by the shaded bars under the temperature profiles.

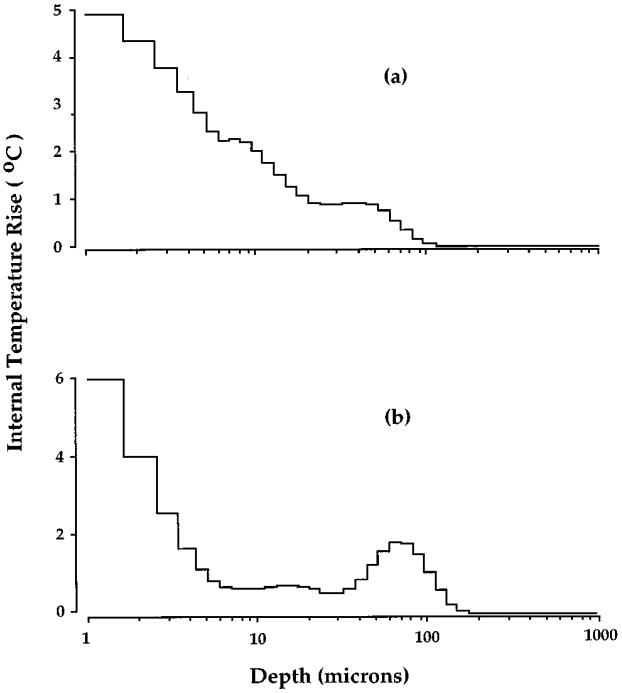

Fig. 10 Depth profiling for skin. The top graph shows the temperature distribution for a healthy area of the skin and the bottom one is for a port wine stain. A temperature peak is evident at around 80 μm, indicating the presence of a subsurface absorber.

4.3 SKIN

Figure 10 shows the results of PPTR experiments conducted on skin using a 577-nm laser. The top figure shows the calculated internal temperature distribution for a healthy area on the wrist. The bottom graph shows the calculated temperature profile for a port wine stain. There is a noticeable peak in the temperature profile at around 80 μm, indicating the presence of a subsurface absorber.

5 DISCUSSION

This paper presents an inverse photothermal method to convert surface temperatures as a function of time into internal temperatures as a function of depth. The technique is based on approximating the integral equation describing the black-body radiation of a laser-irradiated sample with a matrix equation. The resulting least-squares problem is then solved using singular-value decomposition (SVD) of the kernel matrix. This method is fast and involves only a single matrix multiplication after the singular-value decomposition. The only computationally intensive process is the singular-value decomposition of the kernel matrix. Computation of an SVD for 50 times and 40 depths takes less than 5 s on most microcomputers. Once the SVD has been

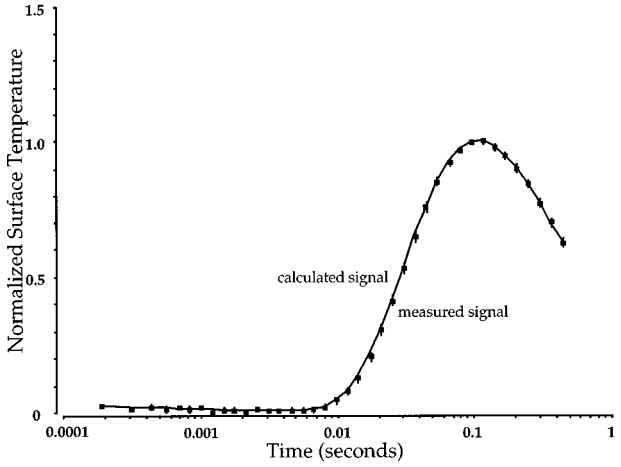

Fig. 11 Identical normalized surface signals from the measured and calculated profiles in Figure 7(b). This figure illustrates multiple solutions to the matrix equation (8).

computed, it does not have to be calculated again since it does not depend on any input data. The SVD can then be stored in memory and used on multiple input files. However, we also acknowledge that we have not performed exhaustive tests comparing the efficiencies of different algorithms.

The algorithm was evaluated using a number of test cases, both simulated and experimental. It worked for homogeneous absorbing and scattering media, and predicted temperatures accurately within 10% up to depths where the temperatures dropped to one-tenth of the maximum value. The technique also predicted temperatures accurately for one case of inhomogeneous media, and that was when the absorbing layer was the first layer of the sample. This was probably because the 170-μm layer was about seven penetration depths thick ($\mu_a = 400\ \mathrm{cm}^{-1}$). This case was therefore not significantly different from a homogeneous absorbing sample.

In the rest of the inhomogeneous samples, the algorithm failed to predict the expected temperatures, as seen in Figures 4, 5, 7(b), and 8. The calculated temperature profile was significantly attenuated and broadened. However, a comparison of the areas under the calculated and expected profiles in Figure 7(b) yielded an equivalent value of 3 mJ/mm^2, which was the radiant exposure used in that case. This implies that the algorithm conserves the energy but spreads it out while calculating temperatures at greater depths. The spreading of the temperature profile may be due to the existence of multiple solution vectors for the matrix equation (8). The multiplicity of the solutions is a consequence of the physics of the thermal interaction, i.e., the two profiles in Figure 7(b) will yield the same radiometric signal at the surface as seen in Figure 11. The internal temperatures generated by the algorithm satisfy the matrix equation (8) mathematically within a specified tolerance; however, the solution generated is not the desired one. It is therefore the severely ill-conditioned thermal inversion problem, and not the algorithm that is the cause of the inaccurate results. This conclusion was also reached by Milner et al., who used different inversion techniques.[17] The technique is fairly efficient at localizing the temperature peaks, but the uncertainty in the depth increases with the depth due to deteriorating resolution.

The final evaluation of the technique used skin, both healthy and with a port wine stain. The results from computer simulations and the inhomogeneous tissue phantoms show that temperatures predicted for subsurface absorbers cannot be accepted as real, but the prediction of their location is reasonable.

Negative temperatures were generated in some of the cases. These are unphysical and emphasize another deficiency of the algorithm. However, we would once again like to emphasize that total energy is conserved (total heat added to the system). The negative temperatures are a result of our unconstrained algorithm for rearranging the energy while trying to achieve a minimum Euclidean norm. It is noteworthy that nearly all the negative temperatures generated are associated with a rapid change in internal temperature, or with large depths. Such changes are likely to create havoc with any fitting process, and negative temperatures are an indication that the algorithm is not working. One simple solution is to set the negative temperatures equal to zero and proceed. More sophisticated approaches, for example, using non-negative least squares[24] or other constraints on the least-squares process, will avoid such problems. While such techniques will force the algorithm to obey physical reality and thus improve the overall accuracy of the results, they still do not do very well at reconstructing sharp features in the solution vector.[18]

This inversion technique is not suitable for resolving two layers relatively close together; the resolution worsens with increasing depth. Based on the impulse response results and the buried layer experiments, a resolution about equal to the depth can be expected, i.e., about 100 μm at a depth of 100 microns.

However, despite these limitations, pulsed photothermal radiometry has the potential to noninvasively probe the first 500 μm of tissue. An important advantage of this method is that no *a priori* knowledge about the tissue is needed. The technique is fast and also works for scattering media since it solves a heat transfer problem and does not rely on rigorous analytical treatment of the light transport in the sample.

Acknowledgments

We thank Dr. Rox Anderson of the Wellman Laboratories of Photomedicine, Massachusetts General

Hospital, for helpful discussions. This work was supported in part by the Collins Foundation, Portland, Oregon.

REFERENCES

1. C. K. Hsieh and J. Lin, ''Solution of inverse heat conduction problems with unknown initial conditions,'' in *Proc. 8th Int. Heat Transfer Conf.* Vol. 2, pp. 609–614 (1986).
2. I. H. Blank, J. Moloney, A. G. Emslie, I. Simon, and C. Apt, ''The diffusion of water across the stratum corneum as a function of its water content,'' *J. Invest. Dermatol.* **82**, 188–194 (1983).
3. A. C. Tam and B. Sullivan, ''Remote sensing applications of pulsed photothermal radiometry,'' *Appl. Phys. Lett.* **43**, 333–335 (1983).
4. W. P. Leung and A. C. Tam, ''Techniques of flash radiometry,'' *J. Appl. Phys.* **56**, 153–161 (1984).
5. W. P. Leung and A. C. Tam, ''Thermal diffusivity in thin films measured by noncontact single-ended pulsed-laser-induced thermal radiometry,'' *Opt. Lett.* **9**, 93–95 (1984).
6. F. H. Long and T. F. Deutsch, ''Pulsed photothermal radiometry of human artery,'' *IEEE J. Quant. Electron.* **QE-23**, 1821–1826 (1987).
7. F. H. Long, N. S. Nishioka, and T. F. Deutsch, ''Measurement of the optical and thermal properties of biliary calculi using pulsed photothermal radiometry,'' *Lasers Surg. Med.* **7**, 461–466 (1987).
8. R. R. Anderson, H. Beck, U. Bruggemann, W. Farinelli, S. Jacques, and J. A. Parrish, ''Pulsed photothermal radiometry in turbid media: internal reflection of backscattered radiation strongly influences optical dosimetry,'' *Appl. Opt.* **28**, 2256–2262 (1989).
9. S. A. Prah, I. A. Vitkin, U. Bruggemann, B. C. Wilson, and R. R. Anderson, ''Determination of optical properties of turbid media using pulsed photothermal radiometry,'' *Phys. Med. Biol.* **37**, 1203–1217 (1992).
10. P. Cielo, ''Pulsed photothermal evaluation of layered materials,'' *J. Appl. Phys.* **56**, 230–234 (1984).
11. D. L. Balageas, J. C. Krapez, and P. Cielo, ''Pulsed photothermal modeling of layered materials,'' *Appl. Opt.* **59**, 348–357 (1986).
12. E. Welsch and D. Ristau, ''Photothermal measurements on optical thin films,'' *Appl. Opt.* **34**, 7239–7253 (1995).
13. F. H. Long, R. R. Anderson, and T. F. Deutsch, ''Pulsed photothermal radiometry for depth profiling of layered media,'' *Appl. Phys. Lett.* **51**, 2076–2078 (1987).
14. I. A. Vitkin, B. C. Wilson, and R. R. Anderson, ''Analysis of layered scattering materials by pulsed photothermal radiometry: application to photon propagation in tissue,'' *Appl. Opt.* **34**, 2973–2982 (1995).
15. T. E. Milner, L. T. Norvang, L. O. Svaasand, N. Tran, B. S. Tanenbaum, and J. S. Nelson, ''Photothermal tomography of subcutaneous chromophores,'' *Proc. SPIE* **2077**, 228–236 (1991).
16. S. L. Jacques, J. S. Nelson, W. H. Wright, and T. E. Milner, ''Pulsed photothermal radiometry of port-wine-stain lesions,'' *Appl. Opt.* **32**, 2439–2446 (1993).
17. T. E. Milner, D. M. Goodman, B. S. Tanenbaum, B. Anvari, and J. S. Nelson, ''Noncontact determination of thermal diffusivity in biomaterials using infrared imaging radiometry,'' *J. Biomedical Opt.* **1**, 92–97 (1996).
18. T. E. Milner, D. M. Goodman, B. S. Tanenbaum, and J. S. Nelson, ''Depth profiling of laser-heated chromophores in biological tissues by pulsed photothermal radiometry,'' *J. Opt. Soc. Am. A* **12**, 1479–1488 (1995).
19. M. J. C. van Gemert, A. J. Welch, and A. P. Amin, ''Is there an optimal laser treatment for portwine stains?'' *Lasers Surg. Med.* **6**, 76–83 (1986).
20. J. W. Valvano and J. Pearce, ''Temperature measurements,'' in *Optical-Thermal Response of Laser-Irradiated Tissue*, A. J. Welch and M. J. C. van Gemert Eds., Plenum Press, New York (1995).
21. H. S. Carslaw and J. C. Jaeger, *Conduction of Heat in Solids*, 2nd ed., Clarendon Press, Oxford (1986).
22. S. A. Prahl, ''Pulsed photothermal radiometry of inhomogeneous tissue,'' in *Life and Earth Sciences*, A. Mandelis, Ed., Vol. 3 of *Progress in Photothermal and Photoacoustic Science and Technology*, SPIE Press, Bellingham, WA (1996).
23. W. H. Press, B. P. Flannery, S. A. Teukolsky, and W. T. Vetterling, *Numerical Recipes: The Art of Scientific Computing*, Cambridge University Press (1986).
24. C. L. Lawson and R. J. Hanson, *Solving Least Squares Problems*, Prentice-Hall, Englewood Cliffs, NJ (1974).
25. H. J. van Staveren, C. J. M. Moes, J. van Marle, S. A. Prahl, and M. J. C. van Gemert, ''Light scattering in Intralipid-10% in the wavelength range of 400–1100 nm. *Appl. Opt.* **31**, 4507–4514 (1991).
26. R. R. Anderson and J. A. Parrish, ''Microvasculature can be selectively damaged using dye lasers: a basic theory and experimental evidence in human skin,'' *Lasers Med. Sci.* **1**, 263–276 (1981).
27. M. J. C. van Gemert, S. L. Jacques, H. J. C. M. Sterenborg, and W. M. Star, ''Skin optics,'' *IEEE Trans. Biomed. Eng.* **36**, 1146–1154 (1989).
28. M. S. Patterson, B. C. Wilson, and R. Graff, ''*In vivo* tests of the concept of photodynamic threshold dose in normal rat liver photosensitized by aluminum chlorosulphonated phthalocyanine,'' *Photochem. Photobiol.* **51**, 343–349 (1990).
29. R. R. Anderson and J. A. Parrish, ''The optics of human skin,'' *J. Invest. Dermatol.* **77**, 13–19 (1981).